Low-Field Microwave-Free Magnetometry Using the Dipolar Spin Relaxation of Quartet Spin States in Silicon Carbide

Oscar Bulancea-Lindvall[1], Matthew T. Eiles[2,*], Nguyen Tien Son[1,†], Igor A. Abrikosov[1], and Viktor Ivády[1,2,3,4,‡]

[1]*Department of Physics, Chemistry and Biology, Linköping University, Linköping SE-581 83, Sweden*

[2]*Max-Planck-Institut für Physik komplexer Systeme, Nöthnitzer Str. 38, Dresden D-01187, Germany*

[3]*Department of Physics of Complex Systems, Eötvös Loránd University, Egyetem tér 1-3, H-1053 Budapest, Hungary*

[4]*MTA-ELTE Lendület "Momentum" NewQubit Research Group, Pázmány Péter, Sétány 1/A, 1117 Budapest, Hungary*

Paramagnetic defects and nuclear spins are the major sources of magnetic-field-dependent spin relaxation in point-defect quantum bits. The detection of related optical signals has led to the development of advanced relaxometry applications with high spatial resolution. The nearly degenerate quartet ground state of the silicon-vacancy qubit in silicon carbide (SiC) is of special interest in this respect, as it gives rise to relaxation-rate extrema at vanishing magnetic field values and emits in the first near-infrared transmission window of biological tissues, providing an opportunity for the development of sensing applications for medicine and biology. However, the relaxation dynamics of the silicon-vacancy center in SiC have not yet been fully explored. In this paper, we present results from a comprehensive theoretical investigation of the dipolar spin relaxation of the quartet spin states in various local spin environments. We discuss the underlying physics and quantify the magnetic field and spin-bath-dependent relaxation time T_1. Using these findings, we demonstrate that the silicon-vacancy qubit in SiC can implement microwave-free low-magnetic-field quantum sensors of great potential.

I. INTRODUCTION

Due to their robustness, sensitivity, and versatility, point-defect quantum bits exhibit enormous potential for quantum sensing. The stringent requirements of emerging multidisciplinary applications, e.g., room-temperature operation, sensing at low or zero magnetic field, microwave-free and all-optical control, and bioinertness, pose numerous challenges for such devices. Novel point-defect sensors that can meet some or all of these criteria are continuously sought after.

The nitrogen-vacancy (N-*V*) center in diamond [1] is the leading contender in quantum sensing applications [2] realized by optically addressable point-defect qubits [3]. Recent developments in N-*V* relaxometry [4–9], where the variation of the longitudinal spin-relaxation time is detected by optical means, have made high-temperature microwave-free sensing applications possible. Sensing at low magnetic field with such sensors is, however, not possible due to the large zero-field splitting of the triplet ground state, which requires a bias field of approximately 100 mT to bring the spin states to near degeneracy. The presence of the bias field is often undesirable, as it may perturb the sample and influence the measurement [10–13].

Relaxometry-based sensing has not been explored for other point-defect qubits, such as the divacancy [14,15] and the negatively charged silicon vacancy [16–18] in silicon carbide (SiC) [15]. The latter defect is, however, attractive for low-magnetic-field relaxometry applications owing to its small zero-field splitting value and resulting quasidegenerate electron spin states. For such applications, a detailed understanding of the relaxation processes of this defect is crucial.

The negatively charged silicon vacancy in SiC provides an optically addressable point defect the quartet ground-state spin [19] of which has a long room-temperature coherence time [20,21]. The unusual high spin state has been utilized in various applications, including quantum sensing [18,22–24], room-temperature masers [25], and

_____
*meiles@pks.mpg.de

†tien.son.nguyen@liu.se

‡viktor.ivady@liu.se

near-infrared quantum information processing [26–28]. In recent years, considerable attention has been paid to experimental characterization of the relaxation dynamics of the quartet silicon-vacancy spin states in a broad temperature range in various SiC samples [21,29,30]. Relaxometry-based sensing schemes have also been proposed for temperature sensing and magnetometry based on the behavior at spin-level anticrossings [31,32]. However, the external field dependence of the relaxation processes due to environmental spin coupling has received little attention thus far but must be understood in detail for various relaxometry applications. Recent theoretical developments have enabled parameter-free calculations of the two major contributions to the longitudinal spin relaxation, namely the temperature-dependent spin-lattice relaxation [33–35] and the magnetic-field-dependent dipolar spin relaxation induced by local environmental spins [15,36,37].

In this paper, we study the magnetic field and local-spin-environment dependence of the dipolar spin relaxation of the V1 and V2 silicon-vacancy centers in the $4H$ polytype of SiC ($4H$-SiC) [38]. We consider various environmental spin species, such as the naturally abundant ^{13}C and ^{29}Si nuclear spins and spin-1/2 and spin-1 point defects, over a wide range of concentrations. We identify the most relevant level anticrossings (LACs), where environmental spins efficiently relax the quartet spin states, and quantify the spin-relaxation time T_1. We find several narrow resonances, where the spin-relaxation time can vary over several orders of magnitude within a small magnetic field interval close to $B = 0$. Utilizing these observations, we propose quantum sensors for biological use and estimate their sensitivity.

The paper is organized as follows. In Sec. II, we detail the models and the simulation technique used. In Sec. III, we present our computational results, while in Sec. IV we discuss our proposal for low-field relaxometry with the silicon-vacancy center in SiC. Finally, in Sec. V, we draw our conclusions.

II. METHODOLOGY

We model the relaxation dynamics of many-spin systems consisting of a quartet silicon-vacancy electron spin and a number environmental spins of different kinds. We consider spin-1/2 ^{13}C and ^{29}Si nuclear spins and doublet and triplet electron spin environments. More information on relevant paramagnetic defects in SiC can be found in Ref. [15]. Nuclear and electron baths are considered independently and calculated separately.

The spin Hamiltonian of the many-body system is given by

$$H = H_0 + \sum_i H_i^x + \sum_i H_{0i}^x + \sum_{i,j} H_{ij}, \quad (1)$$

where the Hamiltonian H_0 of the quartet silicon-vacancy spin includes the zero-field splitting (ZFS) and the Zeeman term (ZE),

$$H_0 = H_{\text{ZFS}} + H_{\text{ZE}} = D\left(S_z^2 - \frac{5}{4}\right) + \left(g_e S_z + g_{3\parallel}\frac{S_+^3 - S_-^3}{4i}\right)\mu_B B_z. \quad (2)$$

In Eq. (2), the ZFS parameter $D = 2.6$ MHz ($D = 35.0$ MHz) for the V1 center (V2 center) in $4H$-SiC [38]. The second term on the right-hand side of Eq. (2) accounts for the linear and nonlinear Zeeman interactions of the silicon-vacancy center, where $g_e = 2.0$, $g_{3\parallel} = 0.6$, and μ_B is the Bohr magneton [18]. The nonlinear Zeeman term is a direct consequence of the threefold rotation symmetry and the high spin state of the defect [18,39].

The Hamiltonian H_i^x in Eq. (1) depends on the considered spin bath and, accordingly, $x = \{n, \text{de}, \text{te}\}$. For nuclear spins, it includes only the nuclear Zeeman interaction term,

$$H_i^n = -g_N \mu_N I_{i,z} B_z, \quad (3)$$

where g_N is the nuclear g factor of either the ^{13}C or the ^{29}Si isotope, μ_N is the nuclear magneton, and $I_{i,z}$ is the doublet nuclear spin z operator. For doublet electron (de) spins, the Hamiltonian includes only the linear Zeeman term,

$$H_i^{\text{de}} = g_e \mu_B S_{i,z} B_z, \quad (4)$$

while for triplet electron (te) spins, the Hamiltonian includes the ZFS and the linear Zeeman term,

$$H_i^{\text{te}} = D_i\left(S_{i,z}^2 - \frac{1}{3}\right) + \frac{E_i}{2}\left(S_+^2 + S_-^2\right) + g_e\mu_B S_{i,z} B_z, \quad (5)$$

where D_i and E_i are the ZFS parameters of triplet spin defect i. In our study, the triplet-spin bath consists of divacancy defects, the ZFS parameters of which can be found in Ref. [40].

The Hamiltonian H_{0i}^x terms in Eq. (1) account for the interaction between the silicon-vacancy center and the environmental spins. For nuclear spins, the coupling term can be written as

$$H_{0i}^n = \mathbf{S}A_i\mathbf{I}_i, \quad (6)$$

where $\mathbf{S}$ and $\mathbf{I}_i$ are the quartet electron spin and spin-1/2 nuclear spin vector operators, respectively, and A_i is the hyperfine tensor determined from *ab initio* density-functional-theory (DFT) calculations. The details of the DFT hyperfine calculations can be found in Ref. [36]. For an electron spin bath, the coupling Hamiltonian term is

equal to the magnetic dipole-dipole coupling and can be written as

$$H_{0i}^{de} = H_{0i}^{te} = -\frac{\mu_0 g_e^2 \mu_B^2}{4\pi r^3} \left(3 \left(\mathbf{S}\hat{\mathbf{r}} \right) \left(\mathbf{S}_i\hat{\mathbf{r}} \right) - \left(\mathbf{S}\mathbf{S}_i \right) \right), \quad (7)$$

where μ_0 is the vacuum permeability, $\mathbf{S}_i$ is either the double or the triplet electron spin operator vector of environmental spin defect i, $\mathbf{r}$ is the distance vector of the silicon vacancy and the paramagnetic defect, with $r = |\mathbf{r}|$ and $\hat{\mathbf{r}} = \mathbf{r}/r$. Finally, the last term on the right-hand side of Eq. (1) accounts for intra-spin-bath couplings. According to our numerical tests, this term does not contribute significantly to spin-relaxation phenomena and it is neglected hereinafter.

In the numerical simulations, we investigate the relaxation dynamics of a central electron spin by utilizing a clustering-based computational method recently developed in Ref. [36] and summarized in Ref. [15]. This method uses an extended Lindbladian to facilitate effective interactions. In this work, we use first-order cluster approximation, i.e., a system of N spins is divided into N subsystems. Each subsystem includes the quartet silicon-vacancy electron spin and one spin from the surrounding spin bath. The spin Hamiltonian of the first order subsystem can be written as

$$\widetilde{H}_i^1 = H_0 + H_i + H_{0i}. \quad (8)$$

Our spin-bath models include either $N = 31$ (spin-1/2 or spin-1) paramagnetic defects or $N = 127$ (^{13}C or ^{29}Si) nuclear spins. According to our previous calculations in 4H-SiC [15] and diamond [36,37], these values ensure that our simulations are converged with respect to the bath size. In order to obtain ensemble-averaged quantities, we carry out averaging over different spin-bath configurations. In all cases, an ensemble of 200 random spin-bath configurations is considered. All configurations correspond to either a given isotope abundance or a given defect-electron-spin concentration. We note that in the nuclear spin-bath calculations, we do not consider those random configurations that contain ^{13}C nuclear spin in the first neighbor shell of the defect. In the electron spin-bath calculations, we exclude spins exceeding 100 MHz in coupling strength, since in such cases the energy-level structure is completely mixed by the strong interaction and the center does not function as a regular silicon-vacancy qubit. These restrictions affect only a marginal part of the random ensemble.

For the different spin environments, we carry out two different time-dependent studies. First, starting from a highly polarized state of the quartet spin and a thermal state of the bath, we simulate the time propagation of the many-spin system over a short period of time, $t = 1\ \mu s$, and study the amount of population transferred from the initial state to the other states of the quartet silicon vacancy.

These qualitative studies shed light on the external parameter dependence of the silicon-vacancy–environment couplings. Furthermore, the results of such calculations may be compared with photoluminescence (PL) studies [15,37]. Second, starting from similar initial states, we carry out long time-evolution simulations to quantitatively study the spin-relaxation time T_1. The simulation time t is tested and optimized for all the considered magnetic field values and spin-bath concentrations. Close to the LACs, we use 0.1 ms, while far away from the LACs, we use up to 1-ms simulation time. Similarly to the simulation time, the time step dt of the time propagation is also optimized. As a general rule, dt is selected in such a way that even the fastest coherent oscillation is well resolved in the simulations. In a sufficiently large spin bath, the initial population of the spin states relaxes as a sum of exponentially decaying modes [29,32], from which the characteristic time scale of the decay (T_1) can be obtained. Here, we note that the simulation time is often much shorter than the T_1 time. Due to the extrapolation, the uncertainty of the calculated T_1 time is expectedly larger for a weakly coupled spin bath, where the decay time may reach seconds. Ensemble spin-relaxation times are obtained by averaging the time-dependent population data over the random spin-bath configurations and then fitting an exponential-decay curve to the obtained ensemble-averaged population data.

Generally, the relaxation should be considered for each mode separately. In the case of the spherical approximation applied to a spin-3/2 spin, the spin density matrix may be expanded into a basis set with separate relaxation rates,

$$\varrho(t) = I/4 + c_D \varrho_D e^{-t/T_D} + c_Q \varrho_Q e^{-t/T_Q} + c_O \varrho_O e^{-t/T_O}, \quad (9)$$

where the I, ϱ_D, ϱ_Q, and ϱ_O form the diagonal part of the spherically invariant multipole expansion basis [29], with separate coefficients $\{c_d, c_Q, c_O\}$ and relaxation times $\{T_d, T_Q, T_O\}$. However, since we mainly simulate the initial part of the decay, our results are likely to capture solely the fastest relaxation modes. Therefore, for the calculations performed in this work, a single exponential-decay model is deemed sufficient for quantitatively extracting characteristic relaxation times.

For high spin defects, the dipolar spin relaxation depends on the initial spin state [30]. For the silicon vacancy, we calculate the spin-relaxation effect starting from two different spin states. The initial population is either evenly distributed in the $m_S = \{-1/2, +1/2\}$ subspace or set completely in the $m_S = -1/2$ state. Since the quartet electron spin is polarized in the $m_S = \{-1/2, +1/2\}$ subspace in the optical excitation cycle, the former initial state is natural for microwave-free applications. High-fidelity initialization in a selected spin state can be achieved by applying a resonant microwave pulse [26].

In all cases, the initial state of the bath spins is set to a thermal state.

III. RESULTS

First, we report on spin-relaxation effects caused by the surrounding nuclear spin bath of the V1 and V2 centers in $4H$-SiC. In order to understand the results of this section, we briefly discuss the magnetic field dependence of the quartet energy levels beforehand. As shown in Fig. 1(a) for the V2 center, the doubly degenerate $m_S = \{-1/2, +1/2\}$ and $m_S = \{-3/2, 3/2\}$ subspaces are split by $2D$ at $B = 0$, due to the ZFS interaction of the C_{3v} symmetric quartet ground state. The magnetic field applied along the three-fold rotation axis of the defect lifts the initial degeneracies and gives rise to nearly linear Zeeman shifts. For a positive magnetic field, the $m_S = -3/2$ level crosses both the $m_S = +1/2$ and the $m_S = -1/2$ levels. Inclusion of a weakly coupled spin-1/2 nuclear spin does not undermine the depicted level structure but, most importantly, its hyperfine interaction gives rise to LACs at the crossings of electronic spin states of $\Delta m_S = \pm 1$. The positions of these LACs are labeled by LAC A and LAC C in Fig. 1(a). Furthermore, second-order effects due to couplings that include two nuclear spins, or a nuclear spin and the nonlinear Zeeman terms, enable quantum jumps of $\Delta m_S = \pm 2$. Such second-order effects give rise to an additional LAC midway between LAC A and LAC C, which is labeled as LAC B in Fig. 1(a). At all of these LACs, enhanced electron spin relaxation is expected due to the nuclear spin couplings.

In order to qualitatively study the magnetic field dependence of nuclear-spin-bath-induced spin relaxation, we carry out time-evolution simulations up to a fixed time and investigate the amount of population transferred from the initial state to the rest of the electron spin states. Figure 1(b) depicts the magnetic field dependence of the obtained population variations for the V1 and the V2 centers for two different initialization conditions denoted by "1/2 ss" and "-1/2 o." The former means initialization in the $m_S = \{-1/2, +1/2\}$ subspace, while the latter means initialization in the $m_S = -1/2$ state only. In all cases, the population lost from the initial state is polynomially reduced as the magnetic field exceeds $B_{\text{LAC C}}$. Note that different initialization conditions give rise to different relaxation pathways. In fact, since initialization in the $m_S = -1/2$ enables relaxation to the $m_S = +1/2$ state also, at larger magnetic fields the corresponding population transfer is twice as large as for 1/2-ss-subspace initialization.

For low magnetic field values, the decay of the initial population is sizable due to the presence of several LACs in the fine energy-level structure in this region. In case of the V2 center, the ZFS parameter of which is $D = 35$ MHz, all three LACs can be identified in the population transfer
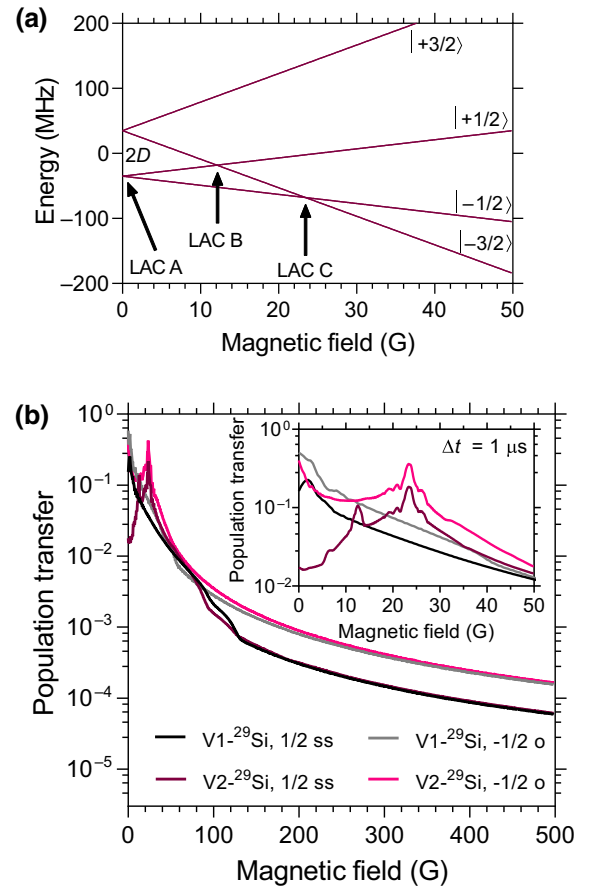

FIG. 1. The energy levels of the V2 center and the nuclear-spin-bath-induced population transfer between the electron spin states of the silicon vacancy. (a) The spin energy levels of an isolated V2 center in $4H$-SiC as a function of the external magnetic field. Due to the zero-field splitting ($2D$) and the Zeeman shift of the states, three crossings can be observed, labeled as LAC A, LAC B, and LAC C. The hyperfine interaction with nearby nuclear spins opens a gap between the crossing states and gives rise to LACs, which enable fast spin flip flops at the corresponding magnetic field values. (b) The population transfer from the initial spin state to the rest of the silicon-vacancy electron spin states. The inset in (b) depicts a close-up of the zero magnetic field region. The electron spin is initialized either in the $m_S = \{+1/2, -1/2\}$ subspace with equal population (labeled as "1/2 ss") or solely in the $m_S = -1/2$ spin state (labeled as "-1/2 o"). The LACs induce efficient spin relaxation that rapidly weakens with increasing magnetic field beyond the positions of the LAC C. The depicted population transfer curves are obtained after a 1-µs-long time evolution of our model system.

plot in Fig. 1(b). Note that LAC A is observed exclusively for the $m_S = -1/2$ initialization condition, while LAC B is observed exclusively when the $m_S = +1/2$ state is also populated. Since the ZFS is $2D = 5.2$ MHz for the V1 center, the LACs can be found very close to $B = 0$ for this center. Due to the width of the LACs, the individual peaks in the population transition curve cannot be resolved.
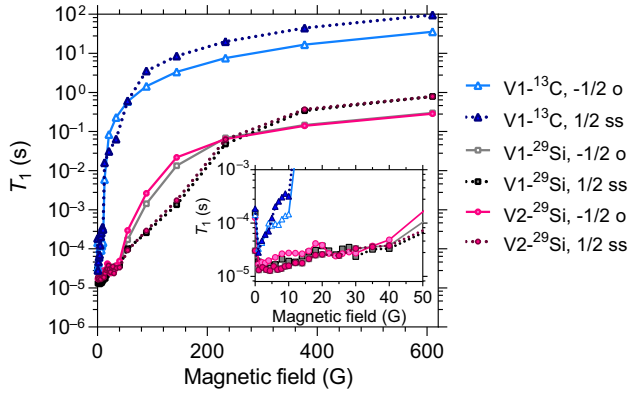
FIG. 2. The magnetic field dependence of the ensemble-averaged spin-relaxation time T_1 of the V1 and V2 centers in 4H-SiC due to hyperfine coupling. The ^{13}C and ^{29}Si nuclear-spin-bath-induced relaxation are provided separately for the V1 center. The solid and dotted lines depict relaxation time curves that correspond to different initialization conditions. For the ^{13}C nuclear spin bath, the spin is initialized in the $m_S = -1/2$ state only (labeled as "-1/2 o"), while for the ^{29}Si nuclear spin bath the spin is initialized in the $m_S = \{1/2, -1/2\}$ subspace, with equal population in the two states (labeled as "1/2 ss"). The inset highlights relaxation times near zero magnetic field.

In order to quantitatively analyze the relaxation mechanism of a silicon-vacancy qubit in the nuclear spin bath of natural and ^{29}Si-depleted 4H-SiC, we carry out large-scale numerical simulations to determine the corresponding T_1 times. Figure 2 summarizes the results of these calculations. For natural samples of 4.68% ^{29}Si and 1.07% ^{13}C isotope content, the relaxation time is determined by the ^{29}Si nuclear spin and the contribution of the paramagnetic ^{13}C spins can be neglected. Indeed, the latter gives rise to a relaxation time that is 2 orders of magnitude larger than that of ^{29}Si, which is the majority nuclear spin source in the sample. Consequently, depletion of the ^{29}Si isotope may give rise to a substantial increase in the relaxation time, when no other relaxation generators, such as electron spins and spin-phonon coupling, are present.

The magnetic field dependence of the T_1 time clearly shows that the LACs drastically reduce the lifetime of the quartet spin in the $B = 0$–60 G interval for both the V1 and the V2 centers. Within this critical region, the T_1 time expectedly limits the coherence time, while outside of this region the T_1 time exceeds 1 ms, and the dipolar spin relaxation no longer limits the coherence time.

Next, we investigate spin-relaxation effects induced by spin-1/2 electron spins (the case of the spin-1 defect environment is briefly discussed in the Appendix). In SiC, there are several different common paramagnetic defects, the concentration of which is determined by the growth conditions and after-growth treatments. The most relevant defects and their expected concentrations in connection

with the spin-relaxation processes of the divacancy qubits in 4H-SiC are summarized in Ref. [15].

As depicted in Fig. 3(a), the fine energy-level structure of a quartet-doublet electron spin pair reveals important differences compared to the energy-level structure seen in Fig. 1(a) for the quartet electron spin system. Since both electron spins exhibit Zeeman splittings with $g \approx 2$ and the zero-field splitting value of the silicon-vacancy qubit is already suppressed at small magnetic field values, the magnetic field dependence of the energy levels of the coupled pair can be interpreted as the sum of a quintet (spin-2) and a triplet (spin-1) subspace. The triplet subspace is nearly degenerate with the three innermost states of the quintet subspace [see Fig. 3(a)]. To be able to keep track of the quartet silicon-vacancy spin states, hereinafter we use the $|m_S m_{S'}\rangle$ notation to label the states. Due to the small but nonzero ZFS of the silicon-vacancy center, four LACs (LAC 1–4) can be found in the vicinity of $B = 0$ [see the inset of Fig. 3(a)]. Furthermore, an additional LAC is found at larger magnetic field values (LAC 5). It occurs due to the nonlinearity of the quartet spin states of the silicon vacancy. We note that the position of LAC 5 may not be well defined in a natural sample, as any inhomogeneity, e.g., due to the local hyperfine fields of the two electron spins, may significantly shift the position of LAC 5.

Our qualitative study for spin-1/2 electron-spin-bath-induced spin relaxation is summarized in Fig. 3(b). When the silicon-vacancy spin is initialized in the $m_S = \{1/2, -1/2\}$ subspace, three narrow resonance peaks correspond to LAC 2–4, while a wide peak at around $B = 380$ G marks the position of LAC 5. The oscillations observable on the sides of the resonance peak of LAC 5 are a side effect of the finite simulation time and the slow coherent oscillations between states $|-3/2, +1/2\rangle$ and $|-1/2, -1/2\rangle$. For the V1 center, all LAC-related resonances occur much closer to $B = 0$.

When the initial population is set in the $m_S = -1/2$ state only, we observe an unexpectedly high nearly magnetic-field-independent population transfer to the empty states [see the dashed lines in Fig. 3(b)]. To understand this observation, we refer to Fig. 3(a), which shows a degenerate pair of states at the zero value of the energy scale. This magnetic-field-independent degenerate subspace includes the $|+1/2, -1/2\rangle$ and the $|-1/2, +1/2\rangle$ states, which can be coupled by the spin flip-flop operator of the dipole-dipole interaction. Since the states are degenerate, even a weak coupling between the two electron spins can give rise to a sizable population transfer within the doublet manifold, which explains the constantly high value in Fig. 3(b). We note that recent measurements have demonstrated fast $|-1/2\rangle \leftrightarrow |+1/2\rangle$ relaxation [30] in accordance with our findings. The phenomenon of efficient spin relaxation between the $|\pm 1/2\rangle$ states and its effects on the decoherence of the V2 center is further investigated in Ref. [41].
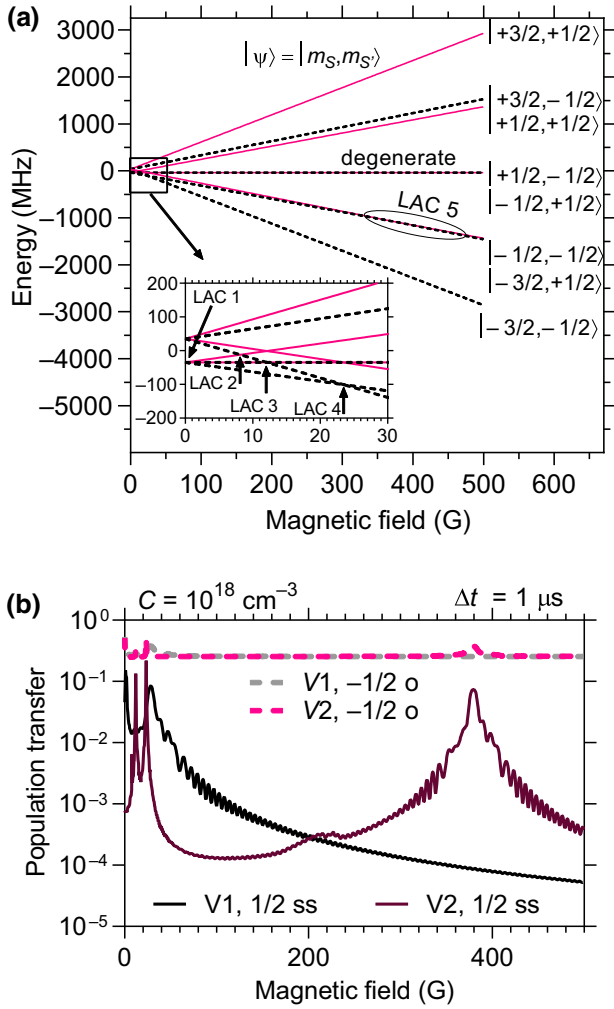
FIG. 3. (a) The energy levels of a quartet-doublet two-electron spin system. The inset shows a close-up of the zero magnetic field region. Altogether, five level anticrossings, marked by LAC 1–5, can be found at distinct magnetic field values. The solid pink and dashed black lines indicate the up and down states of the spin-1/2 defect. (b) The electron-spin-defect-induced population transfer from the highly polarized initial state to the empty quartet spin states of the V1 and V2 centers. The solid and dashed lines depict curves that correspond to different initialization conditions. For the former, the spin is initialized in the $m_S = -1/2$ state only (labeled as "-1/2 o"), while for the latter the spin is initialized in the $m_S = \{1/2, -1/2\}$ subspace, with equal population in the two states (labeled as "1/2 ss"). The concentration for the spin-1/2 defect is set to 10^{18} cm^{-3} and an overall simulation time of 1 μs is used.

Next, we quantitatively investigate the magnetic field dependence of the longitudinal spin-relaxation time of quartet silicon vacancies surrounded by spin-1/2 paramagnetic defects. Figure 4 presents the calculated relaxation time of the V1 and the V2 centers for various spin-bath concentrations. As can be seen, the relaxation time ranges from 100 s to 20 μs, depending on the

concentration of the defects and the magnetic field. As expected, the LACs drastically shorten the lifetime of the silicon-vacancy spins; however, the T_1 time increases rapidly beyond LAC 5.

IV. DISCUSSION

The careful examination of the most relevant spin-relaxation mechanisms of the silicon-vacancy qubit presented in Sec. III allows us to propose a low-magnetic-field relaxometry application, relying on the variation of the spin-state lifetime due to environmental couplings of the silicon-vacancy center in SiC measured through its fluorescence intensity. Such a microwave-free sensor is desirable for various biological applications. Furthermore, the V1 and V2 silicon-vacancy centers with 862-nm and 917-nm zero-phonon photo luminescence emit in the first near-infrared transmission window of biological tissue (650 nm and 950 nm) and thus such a fluorescence silicon-vacancy sensor would also be suitable for *in vivo* applications.

Since the photoluminescence signal of the silicon vacancy depends on the population of the spin states, spin-relaxation-induced population transfers have a direct signature in the optical signal. Under continuous optical excitation, the silicon vacancies are probabilistically excited and the time t spent in the ground state between two excitations follows an exponential distribution. When the center is in the ground state, the initial high degree of polarization in the $m_S = \pm 1/2$ state exponentially decays. Therefore, the PL signal of an ensemble of silicon-vacancy centers is equal to

$$\mathcal{S} = \mathcal{C}\mathcal{I}_0 \int_0^\infty \varrho_{T_d}(t)\, e^{-t/T_1} dt, \tag{10}$$

where $\varrho_{T_d}(t)$ is the probability density function of exponential distribution, T_d is the average dwell time in the ground state for a given excitation power, $\mathcal{C}$ is the spin-dependent contrast of the optical signal, and $\mathcal{I}_0$ is the fluorescence intensity of the defect. Here, we assume that the initialization of the spin state through the optical cycle requires negligible time in comparison with T_d. After integration, the continuous wave signal is equal to

$$\mathcal{S} = \mathcal{C}\mathcal{I}_0 \frac{T_1}{T_1 + T_d} \tag{11}$$

and hence its derivative with respect to the spin-relaxation time is

$$\frac{d\mathcal{S}}{dT_1} = \mathcal{C}\mathcal{I}_0 \left(-\frac{T_1}{(T_1 + T_d)^2} + \frac{1}{T_1 + T_d} \right), \tag{12}$$

which takes its maximal value at $T_1/T_d \to 0$. It is therefore advisable to set the parameters of the silicon-vacancy sensors, the excitation laser power, and the spin-defect
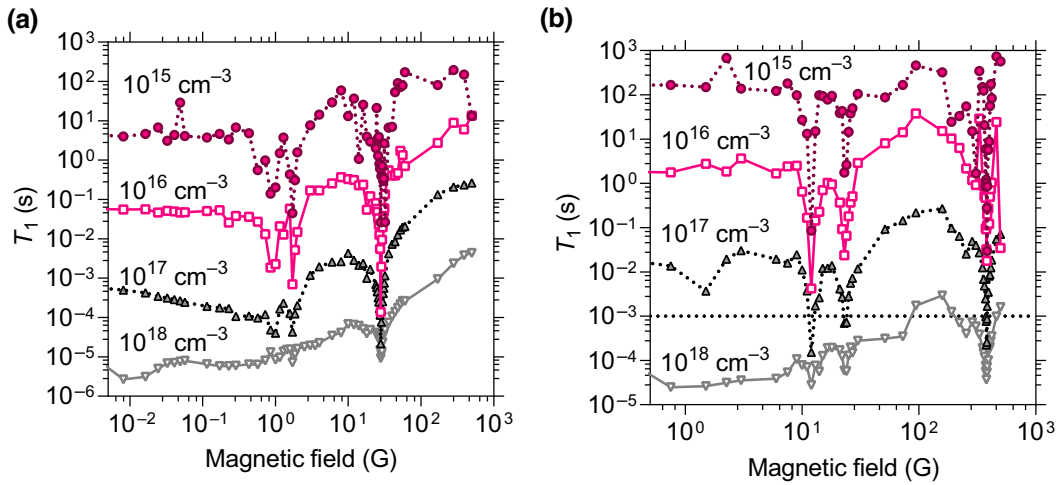
FIG. 4. The magnetic field and electron-spin-defect concentration dependence of the ensemble-averaged spin-relaxation time T_1 of (a) the V1 center and (b) the V2 center. The quartet spin state is initialized in the $m_S = \{1/2, -1/2\}$ subspace. The dashed horizontal line in (b) highlights the typical coherence time for the V2 center.

concentration in such a way that the $T_1 < T_d$ relation is ensured.

Following this model, upon applying a bias field $B_{z,0}$ at the LAC B or C magnetic field regions, monitoring the change in photoluminescence intensity will give an estimate for the relaxation time, which will correspond to a unique value for the external field in the respective monotonous regions of the relaxation time around the LACs. However, to utilize the full LAC region, one may introduce a small oscillating field $B_{z,\omega} = B_\mu \sin(\omega t)$ in addition to the bias, where ω may be well below radio frequency [18]. The external field oscillation will produce an oscillating photoluminescence intensity, with an amplitude and phase difference to the $B_{z,\omega}$ field corresponding to the relaxation time and its derivative, according to

$$\frac{dS}{dt} = \mathcal{C}\mathcal{I}_0 \left(-\frac{T_1}{(T_1 + T_d)^2} + \frac{1}{T_1 + T_d} \right) \frac{dT_1}{dB}\frac{dB_{z,\omega}}{dt}, \quad (13)$$

which can be captured via lock-in measurement. This method will have increasing accuracy with increasing magnetic field sensitivity of the relaxation time and will enable highly sensitive low-field magnetometry in a range of ± 0.3 G according to our predictions (see Fig. 5). To achieve a quantitative accuracy, however, the mapping between PL variation and magnetic field needs to be calibrated for the specific sample and orientation in relation to the c axis of the lattice. Our calculations assume alignment of the external field with the c axis and deviation from this is expected to broaden the relaxation rate peak around each LAC, which could be one way of tuning the sensing range, at the cost of sensitivity [18].

Works using lock-in measurements around the ground-state LAC of the silicon vacancy have reported an accuracy of order 0.1 μT/$\sqrt{\text{Hz}}$ at room temperature when

applied to a silicon-vacancy concentration of $2 \cdot 10^{14}$ cm^{-3} [18,32], which may be limited by the inherent spin contrast and intensity of the silicon-vacancy zero-phonon line. However, this measurement technique is applied in the defect-ensemble setting and increasing the concentration of silicon vacancies would be one way of improving the accuracy. Furthermore, creating silicon vacancies by irradiation will create other defects in the local environment, such as carbon vacancies, in a proportional amount, which will be beneficial in maximizing the LAC relaxation rate due to the electron spin-bath concentration.

Magnetic field sensing can therefore be realized utilizing the magnetic field dependence of the spin-relaxation time $T_1(B)$ studied in this paper. It is important to note, however, that the spin-lattice relaxation induced by
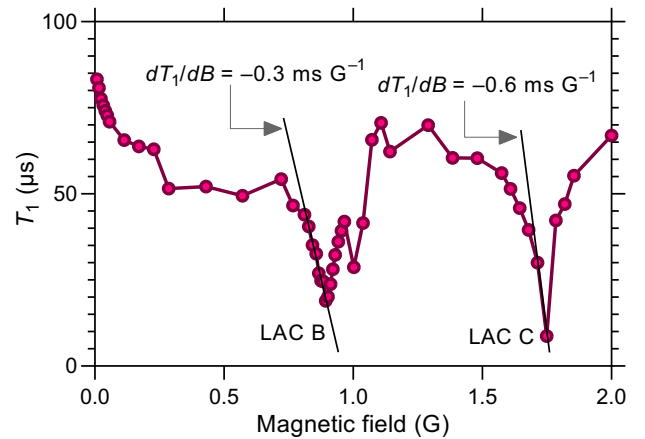

FIG. 5. The spin-relaxation curve of the V1 center at room temperature ($T_1(300\,K) = 100\,\mu$s) for a $C = 10^{17}$ cm^{-3} spin-1/2 point-defect concentration in an isotope-purified 4H-SiC sample.

the magnetic-field-independent spin-orbit and electron-phonon interactions needs to be taken into consideration as well, especially at room temperature. The net relaxation rate can be written as a sum of the two terms,

$$\frac{1}{T_1(B, \mathcal{T})} = \frac{1}{T_1(\mathcal{T})} + \frac{1}{T_1(B)}. \tag{14}$$

Based on recent low-magnetic-field measurements on the silicon-vacancy center in SiC, the spin-lattice relaxation time $T_1(\mathcal{T})$, with $\mathcal{T}$ being the temperature, is in the range of 100 μs at room temperature [21,42]. In order to obtain a measurable magnetic-field-dependent signal, the dipole-dipole-interaction-induced spin-relaxation time $T_1(B)$ needs to be at least in the same order of magnitude. For the V1 (V2) center, this can be achieved at low magnetic field strength by using $C = 10^{17}$ cm^{-3} ($C = 3 \times 10^{17}$ cm^{-3}) spin-1/2 defect concentration in the host material.

In order to achieve the highest sensitivity, the derivative of the relaxation time with respect to the magnetic field $dT_1(B)/dB$ should be maximal. In this respect, the hyperfine interaction that gives rise to local inhomogeneities, variation of the LAC positions, and broadening of the resonance signal is undesirable. Therefore, for high-performance sensing applications, ^{29}Si- (and ^{13}C-) depleted samples are needed. In our calculations, we consider relaxation mechanisms in nuclear and electron spin-bath environments separately; thus our results for spin-1/2 electron spin environments correspond to isotope-purified samples.

The highest gradients can be found close to zero magnetic field at the sharp resonances of the spin-relaxation curves that are associated with LACs in the energy-level structure. In Fig. 5, we depict the $T_1(B, 300 \text{ K})$ curve of the V1 center close to zero magnetic field for a $C = 10^{17}$ cm^{-3} spin-1/2 defect concentration in a paramagnetic isotope-purified 4H-SiC sample. The largest derivative of 0.6 ms G^{-1} is obtained at an external magnetic field value of 1.75 G. Inserting this gradient into Eq. (10), we obtain the variation of the PL signal through the following formula:

$$\frac{1}{\mathcal{C} \mathcal{I}_0} \left| \frac{d\mathcal{S}}{dB} \right| = 4.2 \text{ G}^{-1}. \tag{15}$$

This implies that the PL signal changes by 4.2% of the spin contrast $\mathcal{C}$ for $\Delta B = 1$ μT at $B = 0.175$ mT external field. Such a high gradient may lead to the realization of sensitive dc magnetic field sensors in SiC at very small magnetic field values.

V. CONCLUSIONS

In summary, we comprehensively investigate the dipolar spin relaxation of quartet silicon-vacancy qubits in 4H-SiC. The observed relaxation phenomena significantly differ from the case of triplet qubits in wide-band-gap semiconductors, such as the N-V center in diamond and the divacancy in SiC. Due to the small zero-field splitting, the LACs and most of the strong relaxation processes squeeze into a small magnetic field interval close to $B = 0$. While this region is generally avoided in experiments due to the strong couplings, here we show that one may utilize these effects in room-temperature microwave-free magnetic field sensing applications. Based on our results, we propose that the most suitable 4H-SiC sample for this purpose is a paramagnetic isotope-purified sample that contains spin-1/2 defects in approximately 10^{17} cm^{-3} concentration.

APPENDIX: SPIN RELAXATION DUE TO SPIN-1 DEFECTS

In this appendix, we qualitatively investigate the coupling of the quartet silicon-vacancy spin states to a bath of divacancies. The concentration of these spin-1 defects is not substantial in commonly studied 4H-SiC samples; thus their contribution to the spin-relaxation time may be negligible in most cases. On the other hand, when the electron spin states are resonant, even a few neighboring divacancy centers can give rise to sizable relaxation effects that may be undesirable from the application point of view. To reveal the magnetic field values of the enhanced relaxation due to divacancy spins, we study spin-bath-coupling-induced polarization transfer between the initially polarized and initially empty states over a 1-μs simulation time [for the V1 and V2 centers, see Figs. 6(a) and 6(b)]. Note that the spin bath includes all four possible divacancy configurations; thus Fig. 6 shows the integrated effect of all the different divacancies. As can be seen in
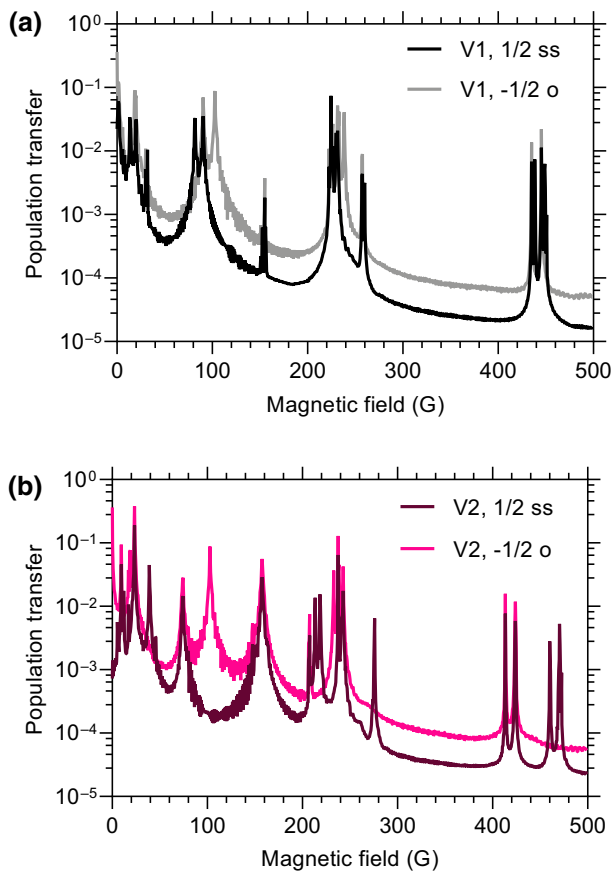
FIG. 6. Population transfer between a silicon vacancy and a bath of divacancy qubits in 4H-SiC. (a),(b) The cases of the V1 and V2 centers, respectively. The dark- and light-color curves show different spin-initialization conditions. In both cases, the figure integrates the contributions from all of the four different divacancy configurations.

Fig. 6, there are numerous resonances due to the multiple crossings between electronic states and the variance of the D_i and E_i ZFS parameters. Furthermore, the relative amplitude of certain resonance peaks may vary depending on the initial spin state of the silicon-vacancy and divacancy qubits.

As can be seen in Fig. 6, the number of resonance peaks drops as the magnetic field increases. In particular, for 300 G $< B <$ 400 G and 500 G $< B$, no resonance peaks can be found. These magnetic field regions may be advantageous for silicon-vacancy applications when both silicon vacancies and divacancy defects are created by positive-ion implantation and subsequent annealing.

[1] M. W. Doherty, N. B. Manson, P. Delaney, F. Jelezko, J. Wrachtrup, and L. C. Hollenberg, The nitrogen-vacancy colour centre in diamond, Phys. Rep. **528,** 1 (2013).

[2] J. F. Barry, J. M. Schloss, E. Bauch, M. J. Turner, C. A. Hart, L. M. Pham, and R. L. Walsworth, Sensitivity optimization for NV-diamond magnetometry, Rev. Mod. Phys. **92,** 015004 (2020).

[3] C. Degen, F. Reinhard, and P. Cappellaro, Quantum sensing, Rev. Mod. Phys. **89,** 035002 (2017).

[4] J.-P. Tetienne, T. Hingant, L. Rondin, A. Cavaillès, L. Mayer, G. Dantelle, T. Gacoin, J. Wrachtrup, J.-F. Roch, and V. Jacques, Spin relaxometry of single nitrogen-vacancy defects in diamond nanocrystals for magnetic noise sensing, Phys. Rev. B **87,** 235436 (2013).

[5] D. Schmid-Lorch, T. Häberle, F. Reinhard, A. Zappe, M. Slota, L. Bogani, A. Finkler, and J. Wrachtrup, Relaxometry and dephasing imaging of superparamagnetic magnetite nanoparticles using a single qubit, Nano Lett. **15,** 4942 (2015).

[6] T. van der Sar, F. Casola, R. Walsworth, and A. Yacoby, Nanometre-scale probing of spin waves using single electron spins, Nat. Commun. **6,** 7886 (2015).

[7] L. T. Hall, P. Kehayias, D. A. Simpson, A. Jarmola, A. Stacey, D. Budker, and L. C. L. Hollenberg, Detection of nanoscale electron spin resonance spectra demonstrated using nitrogen-vacancy centre probes in diamond, Nat. Commun. **7,** 10211 (2016).

[8] T. Rendler, J. Neburkova, O. Zemek, J. Kotek, A. Zappe, Z. Chu, P. Cigler, and J. Wrachtrup, Optical imaging of localized chemical events using programmable diamond quantum nanosensors, Nat. Commun. **8,** 14701 (2017).

[9] A. Finco, A. Haykal, R. Tanos, F. Fabre, S. Chouaieb, W. Akhtar, I. Robert-Philip, W. Legrand, F. Ajejas, K. Bouzehouane, N. Reyren, T. Devolder, J.-P. Adam, J.-V. Kim, V. Cros, and V. Jacques, Imaging non-collinear antiferromagnetic textures via single spin relaxometry, Nat. Commun. **12,** 767 (2021).

[10] H. Zheng, J. Xu, G. Z. Iwata, T. Lenz, J. Michl, B. Yavkin, K. Nakamura, H. Sumiya, T. Ohshima, J. Isoya, J. Wrachtrup, A. Wickenbrock, and D. Budker, Zero-Field Magnetometry Based on Nitrogen-Vacancy Ensembles in Diamond, Phys. Rev. Appl. **11,** 064068 (2019).

[11] T. Lenz, A. Wickenbrock, F. Jelezko, G. Balasubramanian, and D. Budker, Magnetic sensing at zero field with a single nitrogen-vacancy center, Quantum Sci. Technol. **6,** 034006 (2021).

[12] K.-M. C. Fu, G. Z. Iwata, A. Wickenbrock, and D. Budker, Sensitive magnetometry in challenging environments, AVS Quantum Sci. **2,** 044702 (2020).

[13] N. Wang, C.-F. Liu, J.-W. Fan, X. Feng, W.-H. Leong, A. Finkler, A. Denisenko, J. Wrachtrup, Q. Li, and R.-B. Liu, Zero-field magnetometry using hyperfine-biased nitrogen-vacancy centers near diamond surfaces, Phys. Rev. Res. **4,** 013098 (2022).

[14] W. F. Koehl, B. B. Buckley, F. J. Heremans, G. Calusine, and D. D. Awschalom, Room temperature coherent control of defect spin qubits in silicon carbide, Nature **479,** 84 (2011).

[15] O. Bulancea-Lindvall, N. T. Son, I. A. Abrikosov, and V. Ivády, Dipolar spin relaxation of divacancy qubits in silicon carbide, npj Comput. Mater. **7,** 1 (2021).

[16] V. A. Soltamov, A. A. Soltamova, P. G. Baranov, and I. I. Proskuryakov, Room Temperature Coherent Spin

Alignment of Silicon Vacancies in 4*H*- and 6*H*-SiC, Phys. Rev. Lett. **108**, 226402 (2012).

[17] M. Widmann, S.-Y. Lee, T. Rendler, N. T. Son, H. Fedder, S. Paik, L.-P. Yang, N. Zhao, S. Yang, I. Booker, A. Denisenko, M. Jamali, S. A. Momenzadeh, I. Gerhardt, T. Ohshima, A. Gali, E. Janzén, and J. Wrachtrup, Coherent control of single spins in silicon carbide at room temperature, Nat. Mater. **14**, 164 (2015).

[18] D. Simin, V. A. Soltamov, A. V. Poshakinskiy, A. N. Anisimov, R. A. Babunts, D. O. Tolmachev, E. N. Mokhov, M. Trupke, S. A. Tarasenko, A. Sperlich, P. G. Baranov, V. Dyakonov, and G. V. Astakhov, All-Optical dc Nanotesla Magnetometry Using Silicon Vacancy Fine Structure in Isotopically Purified Silicon Carbide, Phys. Rev. X **6**, 031014 (2016).

[19] D. Riedel, F. Fuchs, H. Kraus, S. Väth, A. Sperlich, V. Dyakonov, A. A. Soltamova, P. G. Baranov, V. A. Ilyin, and G. V. Astakhov, Resonant Addressing and Manipulation of Silicon Vacancy Qubits in Silicon Carbide, Phys. Rev. Lett. **109**, 226402 (2012).

[20] M. Widmann, S.-Y. Lee, T. Rendler, N. T. Son, H. Fedder, S. Paik, L.-P. Yang, N. Zhao, S. Yang, I. Booker, A. Denisenko, M. Jamali, S. A. Momenzadeh, I. Gerhardt, T. Ohshima, A. Gali, E. Janzén, and J. Wrachtrup, Coherent control of single spins in silicon carbide at room temperature, Nat. Mater. **14**, 164 (2015).

[21] D. Simin, H. Kraus, A. Sperlich, T. Ohshima, G. V. Astakhov, and V. Dyakonov, Locking of electron spin coherence above 20 ms in natural silicon carbide, Phys. Rev. B **95**, 161201 (2017).

[22] S.-Y. Lee, M. Niethammer, and J. Wrachtrup, Vector magnetometry based on $s = 3/2$ electronic spins, Phys. Rev. B **92**, 115201 (2015).

[23] M. Niethammer, M. Widmann, S.-Y. Lee, P. Stenberg, O. Kordina, T. Ohshima, N. T. Son, E. Janzén, and J. Wrachtrup, Vector Magnetometry Using Silicon Vacancies in 4*H*-SiC under Ambient Conditions, Phys. Rev. Appl. **6**, 034001 (2016).

[24] A. N. Anisimov, D. Simin, V. A. Soltamov, S. P. Lebedev, P. G. Baranov, G. V. Astakhov, and V. Dyakonov, Optical thermometry based on level anticrossing in silicon carbide, Sci. Rep. **6**, 33301 (2016).

[25] H. Kraus, V. A. Soltamov, D. Riedel, S. Väth, F. Fuchs, A. Sperlich, P. G. Baranov, V. Dyakonov, and G. V. Astakhov, Room-temperature quantum microwave emitters based on spin defects in silicon carbide, Nat. Phys. **10**, 157 (2014).

[26] R. Nagy, M. Niethammer, M. Widmann, Y.-C. Chen, P. Udvarhelyi, C. Bonato, J. U. Hassan, R. Karhu, I. G. Ivanov, N. T. Son, J. R. Maze, T. Ohshima, O. O. Soykal, A. Gali, S.-Y. Lee, F. Kaiser, and J. Wrachtrup, High-fidelity spin and optical control of single silicon-vacancy centres in silicon carbide, Nat. Commun. **10**, 1954 (2019).

[27] N. T. Son, C. P. Anderson, A. Bourassa, K. C. Miao, C. Babin, M. Widmann, M. Niethammer, J. Ul Hassan, N. Morioka, I. G. Ivanov, F. Kaiser, J. Wrachtrup, and D. D. Awschalom, Developing silicon carbide for quantum spintronics, Appl. Phys. Lett. **116**, 190501 (2020).

[28] C. Babin, *et al.*, Fabrication and nanophotonic waveguide integration of silicon carbide colour centres with preserved spin-optical coherence, Nat. Mater. **21**, 67 (2022).

[29] V. A. Soltamov, C. Kasper, A. V. Poshakinskiy, A. N. Anisimov, E. N. Mokhov, A. Sperlich, S. A. Tarasenko, P. G. Baranov, G. V. Astakhov, and V. Dyakonov, Excitation and coherent control of spin qudit modes in silicon carbide at room temperature, Nat. Commun. **10**, 1678 (2019).

[30] A. J. Ramsay and A. Rossi, Relaxation dynamics of spin-3/2 silicon vacancies in 4*H*-SiC, Phys. Rev. B **101**, 165307 (2020).

[31] A. N. Anisimov, D. Simin, V. A. Soltamov, S. P. Lebedev, P. G. Baranov, G. V. Astakhov, and V. Dyakonov, Optical thermometry based on level anticrossing in silicon carbide, Sci. Rep. **6**, 33301 (2016).

[32] S. A. Tarasenko, A. V. Poshakinskiy, D. Simin, V. A. Soltamov, E. N. Mokhov, P. G. Baranov, V. Dyakonov, and G. V. Astakhov, Spin and optical properties of silicon vacancies in silicon carbide—a review, Phys. Status Solidi (b) **255**, 1700258 (2018).

[33] J. Gugler, T. Astner, A. Angerer, J. Schmiedmayer, J. Majer, and P. Mohn, *Ab initio* calculation of the spin lattice relaxation time T_1 for nitrogen-vacancy centers in diamond, Phys. Rev. B **98**, 214442 (2018).

[34] J. Park, J.-J. Zhou, and M. Bernardi, Spin-phonon relaxation times in centrosymmetric materials from first principles, Phys. Rev. B **101**, 045202 (2020).

[35] J. Xu, A. Habib, S. Kumar, F. Wu, R. Sundararaman, and Y. Ping, Spin-phonon relaxation from a universal ab initio density-matrix approach, Nat. Commun. **11**, 2780 (2020).

[36] V. Ivády, Longitudinal spin relaxation model applied to point-defect qubit systems, Phys. Rev. B **101**, 155203 (2020).

[37] V. Ivády, H. Zheng, A. Wickenbrock, L. Bougas, G. Chatzidrosos, K. Nakamura, H. Sumiya, T. Ohshima, J. Isoya, D. Budker, I. A. Abrikosov, and A. Gali, Photoluminescence at the ground-state level anticrossing of the nitrogen-vacancy center in diamond: A comprehensive study, Phys. Rev. B **103**, 035307 (2021).

[38] V. Ivády, J. Davidsson, N. T. Son, T. Ohshima, I. A. Abrikosov, and A. Gali, Identification of Si-vacancy related room-temperature qubits in 4*H* silicon carbide, Phys. Rev. B **96**, 161114 (2017).

[39] V. Ivády, I. A. Abrikosov, and A. Gali, First principles calculation of spin-related quantities for point defect qubit research, npj Comput. Mater. **4**, 76 (2018).

[40] A. L. Falk, B. B. Buckley, G. Calusine, W. F. Koehl, V. V. Dobrovitski, A. Politi, C. A. Zorman, P. X.-L. Feng, and D. D. Awschalom, Polytype control of spin qubits in silicon carbide, Nat. Commun. **4**, 1819 (2013).

[41] O. Bulancea-Lindvall, M. T. Eiles, N. T. Son, I. A. Abrikosov, and V. Ivády, Isotope purification induced reduction of spin relaxation and spin coherence times in semiconductors (2022), ArXiv:2205.05105.

[42] H. Singh, A. N. Anisimov, S. S. Nagalyuk, E. N. Mokhov, P. G. Baranov, and D. Suter, Experimental characterization of spin-3/2 silicon vacancy centers in 6*H*-SiC, Phys. Rev. B **101**, 134110 (2020).